RSC Advances

ROYAL SOCIETY OF CHEMISTRY

www.rsc.org/advances

One-pot synthesis of graphene/zinc oxide by microwave irradiation with enhanced supercapacitor performance †

Yanzhen Guo, Binbin Chang, Ting Wen, Chunmei Zhao, Hang Yin, Yannan Zhou, Yonggang Wang, Baocheng Yang*, Shouren Zhang*

Abstract: A facile one-step microwave irradiation method is developed to synthesize the composite of graphene and zinc oxide, which is quick and environmentally friendly. The obtained nanostructured hybrid material was utilized for fabrication of supercapacitor electrode and the electrochemical performance was investigated intensively. The electrode with the as-prepared graphene/zinc oxide composite displayed the specific capacitance as high as 201 F g^{-1} in 1 M Na_2SO_4 at a current density of 1 A g^{-1}, which is much higher than those of pure microwave reduction graphene oxide (77 F g^{-1}) and zinc oxide (5 F g^{-1}) at the same current density. In addition, the specific capacitance of MRGO/ZnO electrode presented an outstanding cycling stability with capacitance retention of 93% even after 3000 cycles. This research provides a feasible method for low-cost manufacture of other graphene-based materials with high-performance applications in energy-storage.

1 Introduction

Supercapacitors, also called ultracapacitors[1] have drawn considerable attention

* Institute of Nanostructured Functional Materials, Huanghe Science and Technology College, Zhengzhou, Henan 450006, China. E-mail: ybc@hhstu.edu.cn, zhangshouren1984@126.com

† Electronic supplementary information (ESI) available.

during recent years due to their fast charge-discharge characteristics, high power density, and excellent cycle stability[2]. Supercapacitors can be classified into two types depending on the energy storage mechanisms: electrical double-layer (EDL) capacitors and pseudocapacitors[3]. EDL capacitors, often selected carbon-based[4] (including activated carbon[5], carbon nanotubes[6], graphene[7], *etc*) materials as the electrode materials, physically store charges via reversible ion adsorption at the electrode-electrolyte interface. On the contrary, pseudocapacitors chemically store charge via redox reactions at the vicinity of the surface while the electrode materials for pseudocapacitors are always metal oxide[8] and conducting polymers[9].

Among the different kinds of carbon-based materials, graphene has emerged as the most appealing material for supercapacitor applications in recent years[10, 11]. Graphene is a one-atom-thick two-dimensional sheet with high conductivity and ultrahigh theoretic surface area (over 2600 m^2 g^{-1}) which facilitates electron transfer between the active materials and the charge collector. Unfortunately, the unavoidable agglomeration of graphene dramatically restricts the surface area, the amount of active sites and impedes the effective electron transfer, resulting in an unsatisfactory capacitive property. Studies have shown that the specific capacitances of graphene can only achieve 135 and 99 F g^{-1} in aqueous and organic electrolytes, respectively[7], far less than the theoretical capacitance of 550 F g^{-1}. In order to reduce the aggregation and thus improve the specific capacitance, many methods have been employed to enhance the supercapacitor performance of graphene-based materials. One way of the methods is the application of a modified

synthesis route. A three-dimensional holey graphene framework with a hierarchical porous structure is synthesized by adding H_2O_2 in the hydrothermal reaction, and the graphene framework electrode delivers a gravimetric capacitance of 298 F g^{-1}[112]. A porous carbon with a Brunauer-Emmett-Teller surface area of 3100 m^2 g^{-1} is obtained by using chemical activation of microwave exfoliated graphite oxide, delivering a specific capacitance of 165 F g^{-1} at a current density of 1.4 A g^{-1}[113]. Similarly, graphene-derived carbons obtained via microwave expansion and KOH activation exhibit a specific capacitance of 174 F g^{-1} in an ionic liquid electrolyte[14]. Additionally, 3D graphene sponges are also reported to improve the capacitance of graphene[15-17]. Another approach to enhance the supercapacitor performance is using pseudocapacitive materials[18](*e.g.* RuO_2[19], MnO_2[20], conductive polymer[21-23], *etc*) as additives to graphene which can decrease the aggregation and restacking of graphene sheets[24, 25], leading the composite obtain a higher specific capacitance.

Zinc oxide, as a wide-band gap semiconductor, has been used as a potential candidate for supercapacitor application for its eco-friendly nature. However, ZnO usually delivers a relatively low specific capacitance due to the poor electrical conductivity and accessible surface areas. Thus ZnO always act as an additives to carbon materials[26, 27], especially for graphene[28, 29]. Graphene/ZnO composite film synthesized by deposition of ZnO on graphene film via ultrasonic spray pyrolysis exhibits a specific capacitance of 61.7 F g^{-1}, which is higher than that of graphene (38.9 F g^{-1})[29]. Li *et al* prepared the composite of graphene-ZnO by hydrothermal process, possessing a high capacitance of 156 F g^{-1} at 5

mV s^{-1}[30]. Now there are more and more methods are proposed to prepare graphene/zinc oxide composites, including hydrothermal[30, 31], solvothermal[32], thermal decomposition[33], supercritical carbon dioxide[34], *etc*. Howerer, the synthetic methods are always time-consuming or need intricate manipulation. Besides, the addition of a chemical reductant, such as hydrazine or $NaBH_4$ is always needed for the reduction of graphene oxide, which is potentially hazardous to human. Therefore, an environmental friendly and facile approach for the synthesis of graphene/ZnO is urged to propose.

Microwave irradiation has been used in the exfoliation and reduction of graphene oxide to form graphene[35, 36], as well as for the preparation of graphene/carbon nanotubes composites[37, 38]. Researches have shown that reduction of graphene oxide by microwave irradiation can improve the specific surface area and enhance the supercapacitor performance[13, 14]. In this work, we report a cost-effective microwave irradiation synthesis method for the production of microwave reduction graphene oxide/zinc oxide (MRGO/ZnO) nanocomposite by just augment a portion of zinc acetate to graphene oxide before the process of microwave irradiation. The as-prepared MRGO/ZnO composite was used as supercapacitor electrode material and exhibited a specific capacitance of 201 F g^{-1} in 1 M Na_2SO_4 at a current density of 1 A g^{-1}, which is much higher than those of pure MRGO (77 F g^{-1}) and ZnO (5 F g^{-1}) under identical test condition. Furthermore, the specific capacitance of MRGO/ZnO electrode displayed an outstanding cycling stability with capacitance retention of 93% after 3000 cycles.

2 Experimental

2.1 Synthesis of MRGO

GO was synthesized from purified natural graphite powder by a modified Hummers method[39]. MRGO was obtained by treated GO pressed powder in a domestic microwave oven for 5 min at 1000 W[36].

2.2 Synthesis of ZnO nanoparticles

ZnO nanoparticles were synthesized as follows: 1.2 g of $Zn(NO_3)_2 \cdot 2H_2O$ was added into 60 mL of deionized water under stirring condition. After the dissolution of $Zn(NO_3)_2 \cdot 2H_2O$, 300 μL of hydrazine hydrate (80 %) was added dropwise in the solution with continuous stirring. The obtained solution was transferred to a 80 mL of Teflonlined autoclave and heated at 160 ℃ for 24 h. ZnO nanoparticles were collected by centrifugation and washed thoroughly with deionized water.

2.3 Synthesis of MRGO/ZnO composite

MRGO/ZnO composite was simply prepared by threating the mixture of GO and $Zn(CH_3COO)_2 \cdot 2H_2O$ under microwave irradiation. GO and $Zn(CH_3COO)_2 \cdot 2H_2O$ mixed with a weight ratio of 2:1 in aqueous solution were grinded in a mortar for about 30 min, until the solvent was fully volatilized. Then the mixture was transferred to a glass vial, placed in a domestic microwave oven. MRGO/ZnO composite was obtained by simple microwave irradiation of the mixture for 5 min at 1000 W.

2.4 Electrochemical measurements

Electrochemical properties of MRGO, ZnO and MRGO/ZnO were measured at room temperature in both three-electrode and two-electrode configurations. In the

three-electrode system, the active materials (MRGO, ZnO or MRGO/ZnO) electrode served as working electrode, platinum plate electrode and Ag/AgCl electrode were used as the counter and reference electrode, respectively. The working electrode was prepared by mixing the as-prepared materials with carbon black and poly(tetrafluoroethylene)(PTFE) in a mass ratio of 8:1:1. After thorough mixing, the slurry was coated onto the nickel foam (1*1 cm^2) and then dried at 80℃ for 12 h in a vacuum oven. The mass of active material for MRGO and MRGO/ZnO loading in each working electrode was about 2 mg, while 5-6 mg for ZnO. All electrochemical measurements were carried out in 1 M Na_2SO_4 aqueous electrolyte at room temperature by using a CHI660D electrochemical workstation. The electrochemical impedance spectroscopy (EIS) was performed at open circuit potential over a frequency range from 0.01 to 100000 Hz. Cyclic voltammetry (CV) curves were performed at a scan rate ranging from 10 to 100 mV s^{-1} with a potential window from -1 to 0 V. The galvanostatic charge-discharge (GCD) measurements were conducted with a current density of 1 to 5 A g^{-1} with the same potential window as that for the CV tests.

The specific capacitance values were calculated from galvanostatic charge-discharge curves according to the following equations:

In a three-electrode system:

$$C = \frac{I\Delta t}{m\Delta V} \quad (1)$$

Where C (F g^{-1}) is the specific capacitance of the electrode material in a three-electrode system, I (A) is the applied current in the measurement, Δt (s) is the discharge time, m (g)

is the mass of active material on the electrode, and ΔV (V) is the voltage change during discharge (excluding the IR drop)[40].

In a two-electrode system:

$$C = 4C_{cell} = 4\frac{I\Delta t}{M\Delta V} \quad (2)$$

Where C_{sp} (F g^{-1}) and C_{cell} (F g^{-1}) are the specific capacitance of single electrode materials and the cell, respectively, M (g) is the total mass of the active materials on both the positive and negative electrodes.

The energy density (E, Wh kg^{-1}) and power density (P, kW kg^{-1}) of the cell were calculated based on the two-electrode configuration according to the following equations:

$$E = \frac{C_{cell}*V_{max}^2}{2*3.6} = \frac{C_{sp}*V_{max}^2}{2*4*3.6} \quad (3)$$

$$P = \frac{E*3.6}{\Delta t} \quad (4)$$

where V_{max} is the voltage at the beginning of discharge, with the factor 3.6 in equation of energy density, the unit of energy density (E) is converted from J g^{-1} to Wh kg^{-1}[41].

2.5 Characterization methods

Scanning electron microscope (SEM) images were obtained using a Quanta 250 FEG FEI at 20 kV without any metal coating. Transmission electron microscope (TEM) images were recorded on a Tecnai G2 20 TEM with an accelerating voltage of 200 kV using a carbon-coated copper grid. X-ray diffraction (XRD) measurements were carried out using a Bruker D8 Advance XRD with Cu-Ka radiation at a scanning rate of 0.02° s^{-1} with 2θ ranging from 5 to 90°. Laser micro-Raman spectra were measured on Renishaw in Via Gloucestershire with a 514.5 nm laser excitation. Fourier transform infrared (FTIR)

spectra were obtained on a Thermo Scientific Nicolet iS5 infrared spectrophotometer using KBr discs, with 32 scans average with scan range of 4000-400 cm^{-1} and at a resolution of 4 cm^{-1}. Brunauer-Emmett-Teller (BET) surface area and pore diameter distribution of the obtained samples were obtained from N_2 adsorption at 77 K using a Micrometric ASAP 2020 system. UV-vis absorption spectra were recorded on a U-4100 UV-Vis-NIR Hitachi spectrometer. Photoluminescence (PL) spectra were performed on a FL-4600 Hitachi spectrofluorometer at an excitation wavelength of 375 nm. Thermo Gravimetric (TG) analysis was conducted on a Perkin- Elmer TG/DTG-6300 instrument in air at a temperature range of 50-800 ℃ with a heating rate of 15 ℃ min^{-1}. Microwave irradiation experiments were carried out in a domestic microwave oven (Midea, China) at 1000 W for 5 min.

3 Results and discussion

3.1 Morphological and structural characterizations

The schematic illustration for the fabrication of MRGO/ZnO composite is shown in Fig. 1. After the synthesis of GO by Hummers method, there was plenty of oxygen containing functional groups including carboxyl, hydroxyl and epoxy existing in GO plane, so the surface charge (zeta potential) of graphene oxide sheets is negative[42]. The oxygenated functional groups in GO plane can act as a nucleation center to reacted with the positively charged zinc ion through electrostatic reaction, which facilitated the contact between GO and zinc acetate[28]. The mixture of GO and zinc acetate was grinded thoroughly, until the powder desiccation. MRGO/ZnO was produced by treated the

mixture in a domestic microwave oven for 5 min at 1000W, which can be visually observed by the color of the mixture become black, as shown in Fig. 2g. In the process of microwave irradiation, the unoxidized graphitic region "impurities" in GO can act as the microwave absorbents and further as a heat source to promote the decomposition of zinc acetate[43]. Under the optimum weight ratio of GO to $Zn(CH_3COO)_2 \cdot 2H_2O$ of 2:1, the preparation of graphene/zinc oxide showed a favorable reproducibility and electrochemical performance.

The morphologies of MRGO, ZnO and MRGO/ZnO were examined by SEM and TEM, as shown in Fig. 2. MRGO with wrinkled edges and 3-5 layers was clearly observed from the images of Fig. 2a-c, which was also reported by our previously work[36]. ZnO nanoparticles synthesized by hydrothermal method were highly crystallized with a diameter range of 50 to 100 nm (Fig. 2d-f). Fig. 2g shows the digital photos of the mixture of GO and $Zn(CH_3COO)_2 \cdot 2H_2O$ before and after microwave treatment, the color of the mixture turned brown to black after microwave irradiation for 5 min at 1000 W, indicating the reduction of graphene oxide and decomposition of $Zn(CH_3COO)_2 \cdot 2H_2O$. ZnO nanoparticles were uniformly dispersed on the surface of graphene, as seen in Fig. 2h-k. The diameter of ZnO nanoparticles in MRGO/ZnO was about 20 nm, much smaller and more uniform than the ZnO nanoparticles synthesized by hydrothermal method. In the HRTEM image of MRGO/ZnO (Fig. 2l), graphene edge of MRGO was clearly observed. An interplanar spacing of 0.26 nm for the lattice fringes corresponds to that of ZnO (002) crystal plane.

TG measurement was carried out to determine the weight ratio of ZnO to graphene in the composites of MRGO/ZnO, as shown in Fig. 3a. The TG and derivative thermogravimetric (DTG) curves afforded information about the degradation extent of MRGO/ZnO. Only one step at about 535 ℃ for mass loss appeared, which is due to the removal of MRGO from the composites. The calculations based on the TG and DTG curves indicated that the ZnO content in MRGO/ZnO was about 50% and the decomposition of MRGO was processed at the temperature of 450-610 ℃.

Fig. 3b shows the XRD patterns of MRGO, ZnO and MRGO/ZnO. After reduction of GO by microwave irradiation, a broad peak at 26.6°appeared in MRGO, manifesting the successful reduction and exfoliation of GO. The XRD pattern of ZnO consists of six characteristic diffraction peaks at 31.8, 34.4, 36.2, 47.5, 56.6 and 62.8^{o}, corresponding to the (100), (002), (101), (102), (110) and (103) planes of the hexagonal ZnO phase (JCPDS 36-1451), respectively. In the XRD pattern of MRGO/ZnO, there was a broad peak at about 26° besides the characteristic peaks of ZnO, indicating the successful combination of MRGO and ZnO.

The structure of MRGO/ZnO was further supported by the FTIR spectrum, as shown in Fig. 3c. The broad absorption band at ~3450 cm^{-1} ascribes to the O-H stretching vibrations of absorbed water on the ZnO surface. The absorption band in the range of 450-460 cm^{-1} can be assigned to the vibrations of Zn-O[44], which can be observed in the spectra of both ZnO and MRGO/ZnO. No stretching vibrations of O-H at ~3400 cm^{-1} are observed in the spectra of MRGO and MRGO/ZnO, indicating the successful reduction

of GO by microwave irradiation. Both the absorption peaks of MRGO and the stretching vibration of Zn-O can be observed in the spectrum of MRGO/ZnO, confirming the successful preparation of MRGO/ZnO.

Raman scattering is highly sensitive to the electronic structure and is an important tool for characterization of carbonaceous materials. For the spectrum of ZnO (Fig. 3d), the intense peak at ~435 cm^{-1} corresponds to non-polar optical phonon E_2, which is the characteristic peak of the hexagonal-crystalline phase ZnO [45, 46], in accordance with the XRD results, while the peak of 1150 cm^{-1} is due to the multiple-phonon scattering processes[47]. G band around 1595 cm^{-1} is related to the phonon vibrations of sp^2 hybridized carbons, while D band at 1345 cm^{-1} is corresponding to the disordered carbon. The intensity ratio I_D/I_G of MRGO/ZnO (0.95) exhibits a higher value than that of MRGO (0.38) due to the increasing disorder of sp^2 contributed by the presence of ZnO in the composite.

The UV-Vis absorption spectra and photoluminescence spectra of as-prepared materials were also collected (Fig. 4). ZnO shows an absorption peak at ~375 nm, which can also be observed in MRGO/ZnO, while MRGO exhibits no obvious peak in the range of 200-800 nm. PL spectra of the as-synthesized materials were characterized to examine the optical properties. With the excitation wavelength of 375 nm, an emission peak at ~430 nm was appeared in ZnO, which can also be found in MRGO/ZnO. Two other weak emission peaks at ~490 and 535 nm ascribed to oxygen-vacancies were clearly observed in ZnO, while indiscoverable in the nanocomposite, implying few defects and highly

crystalline of ZnO in MRGO/ZnO composites [34].

Fig. 5 presents the N_2 adsorption-desorption isotherm and pore size distribution of MRGO, ZnO and MRGO/ZnO. MRGO (Fig. 5a) displays a typical type IV isotherm with a clear H3 hysteresis loop, indicative of the existence of flakiness structure with slit pore. Meanwhile, the large adsorption quantity of nitrogen implies a high surface area of 465.7 m^2/g for MRGO, which favors the obtaining of a satisfactory surface area of MRGO/ZnO. As expected, MRGO/ZnO (Fig. 5c) exhibits the type IV isotherms with a H4 hysteresis loop at a relative pressure from 0.4 to 1.0, indicating the generation of porous structure with a wide pore size. More importantly, MRGO/ZnO possesses a prominent surface area of 109.5 m^2/g, which is much higher than those of pure ZnO (9.2 m^2/g) and even the reported value of G-ZnO (7.9 m^2/g)[48]. The pore size distribution of MRGO/ZnO (the insert Fig. 5c) shows that there are two types of pore existing in the framework structure. The primary pore is typical mesopore with 2.43 nm size, which should be attributed to the interspaces between the layers of graphene sheets, and this result is consistent with pore wide of MRGO (the insert Fig. 5a). Another larger pore is mesopore with a widen pore distribution of 7.6-12.8 nm size, which is probably related to the space between the sheets in ZnO nanoparticles. Thus, the satisfactory surface area and superior porosity of MRGO/ZnO endow the advantage for the efficient electron adsorption and transfer.

3.2 Electrochemical behavior

The capacitance of a supercapacitor is strongly dependent on the cell configuration used for the electrochemical test and it is always higher when using a three-electrode than

two-electrode system [49]. In this work, a three-electrode system was first used to evaluate the electrochemical properties of the samples. The CV curves of MRGO/ZnO composite with different scan rates in 1 M Na_2SO_4 are shown in Fig. 6a. CV curves of the composite display quasi rectangular shape without obvious redox peaks, indicating the ideal EDL capacitive behavior. With the increasing of scan rates, CV curves of MRGO/ZnO composite still maintain a nearly rectangular shape, demonstrating a favorable high-rate performance. Galvanostatic charge–discharge curves of MRGO/ZnO electrode with different current densities are shown in Fig. 6b. All the charge and discharge curves present approximately symmetrical triangular shapes with the current density ranging from 1 to 5 A g^{-1}, manifesting MRGO/ZnO possesses excellent electrochemical reversibility, which is consistent with the CV results. CV curves with different scan rates，GCD curves with different current densities of single component of MRGO or ZnO were also investigated, as shown in Fig. S1†. The GCD curve of MRGO/ZnO electrode at 1 A g^{-1} is much larger than those of MRGO and ZnO electrodes (Fig. 6c), indicating significantly improved capacitive properties of the electrode. Correspondingly, the specific capacitance (201 F g^{-1}) of the MRGO/ZnO electrode, which is calculated from the galvanostatic charge-discharge curve, reaches about 3 times higher than that of MRGO (77 F g^{-1}) and much higher than the specific capacitance of ZnO (5 F g^{-1}). To emphasize the structural advantages of our composites, the specific capacitance of our MRGO/ZnO is comparable to previous reports of graphene-ZnO electrode, which are shown in Table 1. The electrode of our sample displayed a higher capacitance with

favorable electrochemical performance. Fig. 6d shows the specific capacitance of ZnO, MRGO and MRGO/ZnO electrode materials as a function of current density. The specific capacitance of MRGO/ZnO still remains as high as 153 F g^{-1} even at a high current density of 5 A g^{-1}, suggesting an admirable rate capability, which is much better than that of MRGO (13 F g^{-1} at 5 A g^{-1}). The effect of various loading on the electrochemical properties of MRGO/ZnO was also inspected. When the weight ratio of graphene oxide to $Zn(CH_3COO)_2 \cdot 2H_2O$ is deviated from the optimum ratio of 2:1, for that of 1:1 and 4:1, the composites showed a less uniform morphology and an unfavorable electrochemical performance which is due to the deficient exertion of graphene or ZnO (Fig. S2† and Table S1). While the weight of graphene oxide was further decreased to 1/2 for that of $Zn(CH_3COO)_2 \cdot 2H_2O$, the composites of MRGO/ZnO cannot be gained on account of the lack of microwave absorbents. The results of Fig. 6 reveal that the incorporation of ZnO into MRGO can greatly improve the capacitive performance of the sample, which can be attributed to case as follows: (1) 2D structure of graphene allows for the uniform distribution of ZnO, which provides larger electrochemically active surface areas for charge transfer than that of ZnO; (2) The existence of ZnO and the wrinkle nature of graphene facilitate the ion diffusion during charge/discharge process; (3) The pseudocapacitance obtained from the reaction between ZnO and Na_2SO_4 electrolyte, which is mainly result from the intercalation and deintercalation of Na^+ from electrolyte into ZnO:[28] $ZnO+Na^++e^- \leftrightarrow ZnONa$ enlarged the CV loops. In general, the introduction of ZnO may allow comprehensive utilization of the EDL capacitance of graphene and

pseudocapacitance of ZnO to produce synergistic effects.

In order to further understand the electrochemical behavior of the samples, EIS measurements are performed (Fig. 7). In the complex plane, the imaginary component, Z" shows the capacitive property while the real component, Z' displays the ohmic property. In the high-frequency region, the real axis intercept represents the equivalent series resistance (ESR), which is the sum of resistance of the electrolyte, the contact resistance of the interface active material/current collector and the intrinsic resistance of the active material [55]. The ESR value of MRGO obtained from the x-intercept is 0.65 Ω, which endows that of MRGO/ZnO (1.16 Ω) lower than ESR of ZnO (1.55 Ω). At low frequency, the imaginary part sharply increases and a nearly vertical line is observed, indicating an ideal EDL capacitive electrode material[56]. The Warburg curve of MRGO/ZnO at low frequency is shorter than that of MRGO and ZnO, indicating lower electronic resistance and faster ion diffusion in the sample. In the medium frequency domain, a small semicircle reflecting the electrochemical reaction impedance of the electrode is observed, and a smaller semicircle means smaller charge transfer resistance[57, 58]. It is apparent that the charge transfer resistance for MRGO (~0.82 Ω) and MRGO/ZnO (~1.14 Ω) are much lower than that of ZnO (~3.41 Ω). The low ESR is crucial for enhancing rate capability or the power density of the electrochemical capacitors since the power density is inversely to ESR[57].

Furthermore, we studied the durability of the electrode materials using galvanostatic charge-discharge measurement at a current density of 2 A g^{-1} for 3000 cycles, as shown

in Fig. 8. It is clear that the specific capacitance still remains of 165 F g^{-1} (about 93% of the initial capacitance) after 3000 cycles, which indicates that MRGO/ZnO displays a good cycling and stable energy-storage process as the supercapacitive electrode material. However, the capacitance retention of MRGO and ZnO remains only for 90% and 48%, respectively. The inset of Fig. 8 shows the galvanostatic charge–discharge curve of MRGO/ZnO electrode at a current density of 2 A g^{-1} , all the curves are linear, symmetrical and no obvious IR drop is observed, illustrating a low thermal resistance owing to the well-formed electrode/electrolyte interface[34].

A two-electrode test cell can provide more accurate measurement of the materials performance for supercapacitor[49, 59]. Therefore, the supercapacitor performance of the samples was further investigated by a symmetrical two-electrode system. The CV curves of MRGO/ZnO composite with different scan rates ranging from 10 to 100 mV s^{-1} are shown in Fig. 9a. CV curves of the composite show rectangular shape even when the scan rate increases up to 100 mV s^{-1}, indicating the ideal capacitive behavior, which is consistent with the results in three-electrode system. Fig. 9b shows the GCD curves of MRGO/ZnO with different current densities. The symmetrical triangular shape of the curves suggests the excellent electrochemical reversibility of the material. The specific capacitance of the composite calculated from the galvanostatic charge-discharge at 1 A g^{-1} is 125 F g^{-1}, which is lower than the value of 201 F g^{-1} based on three-electrode configuration. This phenomenon has been observed in the previous reports [59, 60], which can be attributed to the distinct electrode polarization effect in different electrodes. The

CV curves at a scan rate of 50 mV s^{-1} for the samples were as well collected, as shown in Fig. 9c. The encircled surface of the CV curve for MRGO/ZnO is much larger than those of MRGO and ZnO, indicating significantly improved capacitive properties of the material, which is also observed in the GCD curves in Fig. 9c. EIS spectra of the electrode materials in a symmetric cell were also provided in Fig. S3†, and the shape of the curves is similar to that in three-electrode system. As two of the most primary parameters to determine the energy storage capability for supercapacitors, energy and power density are estimated and presented in Fig. 9d. MRGO/ZnO delivers energy density of 4.37 and 3.06 Wh kg^{-1} with the corresponding power density of 0.53 and 3.42 kW kg^{-1} at 1 and 5 A g^{-1}, higher than that of the pure MRGO powder electrode (1.35 Wh kg^{-1} with the power density of 0.57 kW kg^{-1} at 1 A g^{-1}). Nevertheless, MRGO presents a power density of 5 kW kg^{-1} at 5 A g^{-1}, higher than that of MRGO/ZnO (3.42 kW kg^{-1}), which is due to the lower ESR of MRGO. Such results clearly demonstrate the preferable cycling stability and high specific capacitance of our materials for high-performance supercapacitors.

4 Conclusions

In summary, we have demonstrated a facile, one-step microwave irradiation synthesis of MRGO/ZnO for supercapacitor application. The composite served as a supercapacitor electrode shows high specific capacitance (201 F g^{-1} at 1 A g^{-1}) and excellent rate capability, which is much higher than that of pure MRGO (77 F g^{-1}) and zinc oxide (5 F g^{-1}) at the same current density. More importantly, the specific

capacitance of MRGO/ZnO electrode displays an outstanding cycling stability with capacitance retention of 93% after 3000 cycles. In addition, MRGO/ZnO delivers energy density of 4.37 Wh kg^{-1} with the corresponding power density of 8.33 kW kg^{-1} at 1 A g^{-1}, which is much higher than that of the pure MRGO electrode. Based on this, the preparation method and electrochemical measurement results are potentially efficient for preparation of other graphene-based composites in order to meet diverse energy-storage application requirements.

Acknowledgements

This work was supported by the Natural Science Foundation of China (51472102), New Century Excellent Talents in University (NCET-12-0696), the Leading Talents for Zhengzhou Science and Technology Bureau (Grant no. 131PLJRC649), the program for University Innovative Talents of Science and Technology in Henan Province (Grant no. 2012HASTIT03).

References

1. W. Gu and G. Yushin, *Wiley Interdisciplinary Reviews: Energy and Environment*, 2014, **3**, 424-473.
2. Z. Yu, L. Tetard, L. Zhai and J. Thomas, *Energy Environ. Sci.*, 2015, **8**, 702-730.
3. C. Liu, Z. Yu, D. Neff, A. Zhamu and B. Z. Jang, *Nano letters*, 2010, **10**, 4863-4868.
4. E. Frackowiak and F. Beguin, *Carbon*, 2001, **39**, 937-950.
5. C. Liang, Z. Li and S. Dai, *Angewandte Chemie International Edition*, 2008, **47**, 3696-3717.
6. H. Pan, J. Li and Y. P. Feng, *Nanoscale research letters*, 2010, **5**, 654-668.
7. M. D. Stoller, S. Park, Y. Zhu, J. An and R. S. Ruoff, *Nano letters*, 2008, **8**, 3498-3502.
8. S. Chen, J. Zhu, X. Wu, Q. Han and X. Wang, *ACS nano*, 2010, **4**, 2822-2830.
9. M. Mastragostino, C. Arbizzani and F. Soavi, *Journal of power sources*, 2001, **97**, 812-815.
10. C. Zheng, X. Zhou, H. Cao, G. Wang and Z. Liu, *Journal of power sources*, 2014, **258**, 290-296.
11. M. Lee, B.-H. Wee and J.-D. Hong, *Advanced Energy Materials*, 2015, **5**, n/a-n/a.
12. Y. Xu, Z. Lin, X. Zhong, X. Huang, N. O. Weiss, Y. Huang and X. Duan, *Nature communications*, 2014, **5**.
13. Y. Zhu, S. Murali, M. D. Stoller, K. Ganesh, W. Cai, P. J. Ferreira, A. Pirkle, R. M. Wallace, K. A. Cychosz and M. Thommes, *Science*, 2011, **332**, 1537-1541.
14. T. Kim, G. Jung, S. Yoo, K. S. Suh and R. S. Ruoff, *ACS nano*, 2013, **7**, 6899-6905.
15. X. Xu, L. Pan, Y. Liu, T. Lu, Z. Sun and D. H. Chua, *Scientific reports*, 2015, **5**, 8458.
16. X. Xu, L. Pan, Y. Liu, T. Lu and Z. Sun, *Journal of colloid and interface science*, 2015, **445**, 143-150.
17. J.-Y. Hong, J. J. Wie, Y. Xu and H. S. Park, *Physical Chemistry Chemical Physics*, 2015, DOI: 10.1039/C5CP04203H.
18. U. Patil, S. C. Lee, S. Kulkarni, J. S. Sohn, M. S. Nam, S. Han and S. C. Jun, *Nanoscale*, 2015, **7**, 6999-7021.
19. Y. Yang, Y. Liang, Y. Zhang, Z. Zhang, Z. Li and Z. Hu, *New J. Chem.*, 2015, **39**, 4035-4040.
20. Z. Yu, B. Duong, D. Abbitt and J. Thomas, *Advanced materials*, 2013, **25**, 3302-3306.
21. C. Xu, J. Sun and L. Gao, *Journal of Materials Chemistry*, 2011, **21**, 11253.
22. Y. Zhao, J. Liu, Y. Hu, H. Cheng, C. Hu, C. Jiang, L. Jiang, A. Cao and L. Qu, *Advanced materials*, 2013, **25**, 591-595.
23. H.-H. Chang, C.-K. Chang, Y.-C. Tsai and C.-S. Liao, *Carbon*, 2012, **50**, 2331-2336.
24. J. Yan, Z. Fan, T. Wei, W. Qian, M. Zhang and F. Wei, *Carbon*, 2010, **48**, 3825-3833.
25. Y. Liu, H. Wang, J. Zhou, L. Bian, E. Zhu, J. Hai, J. Tang and W. Tang, *Electrochimica Acta*, 2013, **112**, 44-52.
26. M. Selvakumar, D. K. Bhat, A. M. Aggarwal, S. P. Iyer and G. Sravani, *Physica B: Condensed Matter*, 2010, **405**, 2286-2289.
27. Y. Zhang, X. Sun, L. Pan, H. Li, Z. Sun, C. Sun and B. K. Tay, *Journal of Alloys and Compounds*, 2009, **480**, L17-L19.
28. Y.-L. Chen, Z.-A. Hu, Y.-Q. Chang, H.-W. Wang, Z.-Y. Zhang, Y.-Y. Yang and H.-Y. Wu, *The Journal of Physical Chemistry C*, 2011, **115**, 2563-2571.

29. T. Lu, Y. Zhang, H. Li, L. Pan, Y. Li and Z. Sun, *Electrochimica Acta*, 2010, **55**, 4170-4173.
30. Z. Li, Z. Zhou, G. Yun, K. Shi, X. Lv and B. Yang, *Nanoscale research letters*, 2013, **8**, 1-9.
31. A. R. Marlinda, N. M. Huang, M. R. Muhamad, M. N. An'amt, B. Y. S. Chang, N. Yusoff, I. Harrison, H. N. Lim, C. H. Chia and S. V. Kumar, *Materials Letters*, 2012, **80**, 9-12.
32. J. Wu, X. Shen, L. Jiang, K. Wang and K. Chen, *Applied Surface Science*, 2010, **256**, 2826-2830.
33. Z. Li, P. Liu, G. Yun, K. Shi, X. Lv, K. Li, J. Xing and B. Yang, *Energy*, 2014, **69**, 266-271.
34. Y. Haldorai, W. Voit and J.-J. Shim, *Electrochimica Acta*, 2014, **120**, 65-72.
35. Y. Zhu, S. Murali, M. D. Stoller, A. Velamakanni, R. D. Piner and R. S. Ruoff, *Carbon*, 2010, **48**, 2118-2122.
36. B. Yang, Y. Guo, S. Zhang, T. Wen and C. Zhao, *RSC Advances*, 2014, **4**, 64771-64780.
37. S.-H. Bae, K. Karthikeyan, Y.-S. Lee and I.-K. Oh, *Carbon*, 2013, **64**, 527-536.
38. S.-H. Lee, V. Sridhar, J.-H. Jung, K. Karthikeyan, Y.-S. Lee, R. Mukherjee, N. Koratkar and I.-K. Oh, *ACS nano*, 2013, **7**, 4242-4251.
39. S. Park, J. An, R. D. Piner, I. Jung, D. Yang, A. Velamakanni, S. T. Nguyen and R. S. Ruoff, *Chemistry of Materials*, 2008, **20**, 6592-6594.
40. B. Chang, Y. Guo, Y. Li, H. Yin, S. Zhang, B. Yang and X. Dong, *Journal of Materials Chemistry A*, 2015, **3**, 9565-9577.
41. J. Zhao, H. Lai, Z. Lyu, Y. Jiang, K. Xie, X. Wang, Q. Wu, L. Yang, Z. Jin and Y. Ma, *Advanced materials*, 2015, **27**, 3541-3545.
42. D. Li, M. B. Mueller, S. Gilje, R. B. Kaner and G. G. Wallace, *Nature nanotechnology*, 2008, **3**, 101-105.
43. H. Hu, Z. Zhao, Q. Zhou, Y. Gogotsi and J. Qiu, *Carbon*, 2012, **50**, 3267-3273.
44. B. Li and H. Cao, *journal of materials chemistry*, 2011, **21**, 3346-3349.
45. J. F. JURADO, C. Vargas Hernandez and R. A. VARGAS, *Dyna*, 2012, **79**, 79-85.
46. J. Li and H. Li, *Nanoscale research letters*, 2009, **4**, 165-168.
47. X.-Y. Ye, Y.-M. Zhou, Y.-Q. Sun, J. Chen and Z.-Q. Wang, *Journal of Nanoparticle Research*, 2009, **11**, 1159-1166.
48. S. Liu, H. Sun, A. Suvorova and S. Wang, *Chemical Engineering Journal*, 2013, **229**, 533-539.
49. Q. Cheng, J. Tang, J. Ma, H. Zhang, N. Shinya and L.-C. Qin, *Physical Chemistry Chemical Physics*, 2011, **13**, 17615-17624.
50. Y.-Z. Liu, Y.-F. Li, Y.-G. Yang, Y.-F. Wen and M.-Z. Wang, *Scripta Materialia*, 2013, **68**, 301-304.
51. Y. Zhang, H. Li, L. Pan, T. Lu and Z. Sun, *Journal of Electroanalytical Chemistry*, 2009, **634**, 68-71.
52. A. Ramadoss and S. J. Kim, *Materials Chemistry and Physics*, 2013, **140**, 405-411.
53. J. Wang, Z. Gao, Z. Li, B. Wang, Y. Yan, Q. Liu, T. Mann, M. Zhang and Z. Jiang, *Journal of Solid State Chemistry*, 2011, **184**, 1421-1427.
54. T. Lu, L. Pan, H. Li, G. Zhu, T. Lv, X. Liu, Z. Sun, T. Chen and D. H. Chua, *Journal of Alloys and Compounds*, 2011, **509**, 5488-5492.
55. L. Wei, M. Sevilla, A. B. Fuertes, R. Mokaya and G. Yushin, *Advanced Functional Materials*, 2012, **22**, 827-834.
56. S. Ye and J. Feng, *ACS applied materials & interfaces*, 2014, **6**, 9671-9679.

57. L. Yang, S. Cheng, Y. Ding, X. Zhu, Z. L. Wang and M. Liu, *Nano letters*, 2011, **12**, 321-325.
58. L.-F. Chen, X.-D. Zhang, H.-W. Liang, M. Kong, Q.-F. Guan, P. Chen, Z.-Y. Wu and S.-H. Yu, *ACS nano*, 2012, **6**, 7092-7102.
59. M. D. Stoller and R. S. Ruoff, *Energy & Environmental Science*, 2010, **3**, 1294-1301.
60. V. Khomenko, E. Frackowiak and F. Béguin, *Electrochimica Acta*, 2005, **50**, 2499-2506.

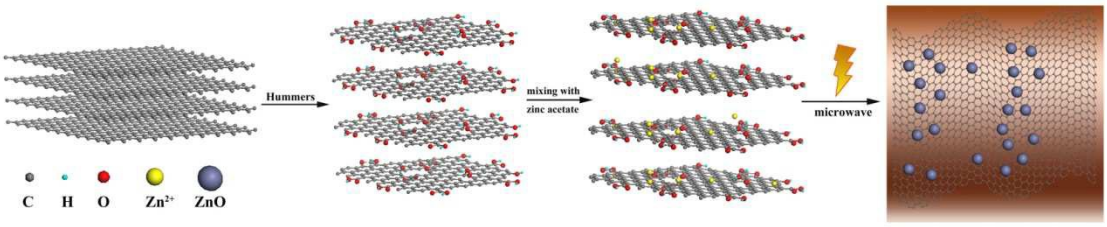

Fig.1 Schematic illustration for the fabrication route of MRGO/ZnO composite.

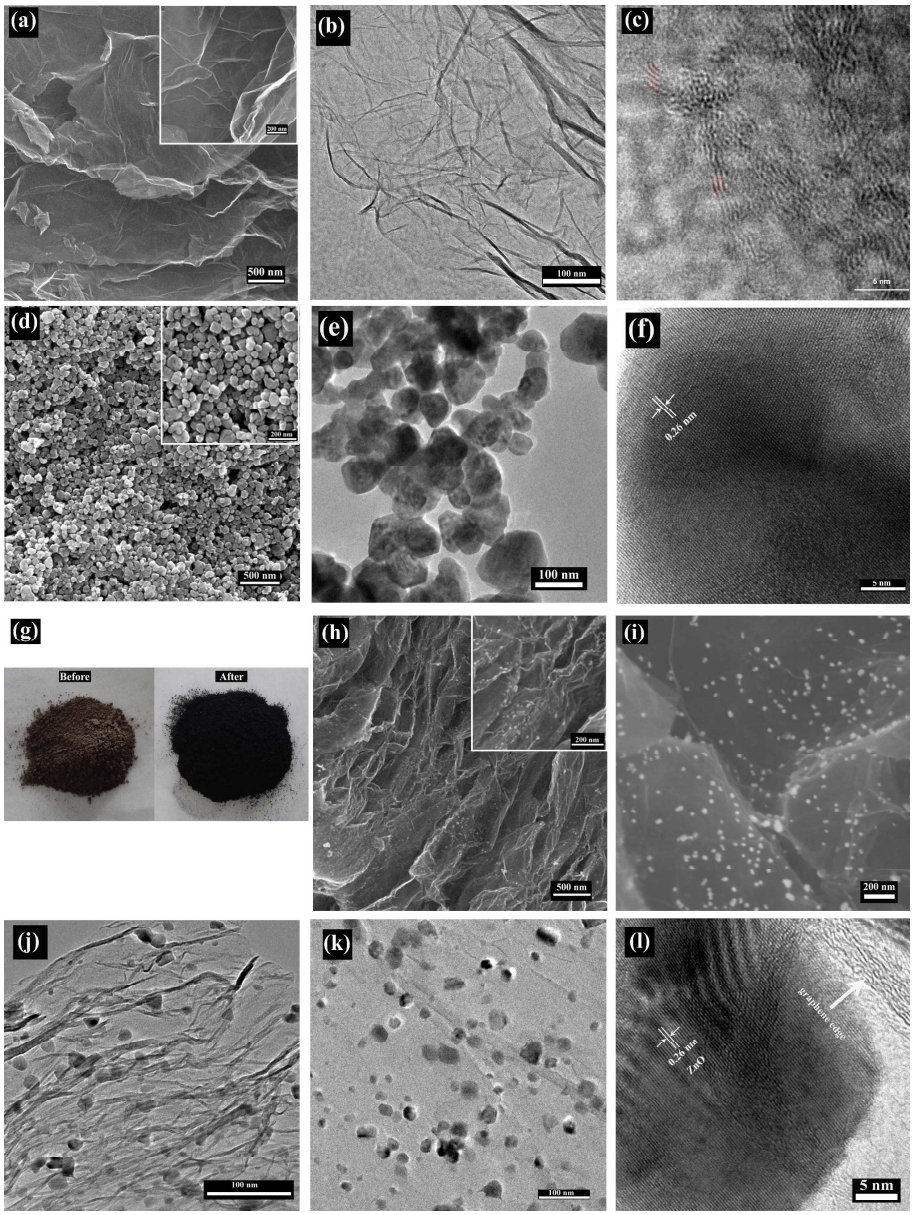

Fig. 2 SEM (a), TEM (b), and HRTEM (c) images of MRGO; SEM (d), TEM (e), and HRTEM (f) images of ZnO; (g) Digital photos of the mixture of GO and $Zn(CH_3COO)_2 \cdot 2H_2O$ before and after microwave irradiation. SEM (h, i), TEM (j, k) and HRTEM (l) images of MRGO/ZnO. Inset of a, d, h are the high-magnification SEM images of the samples.

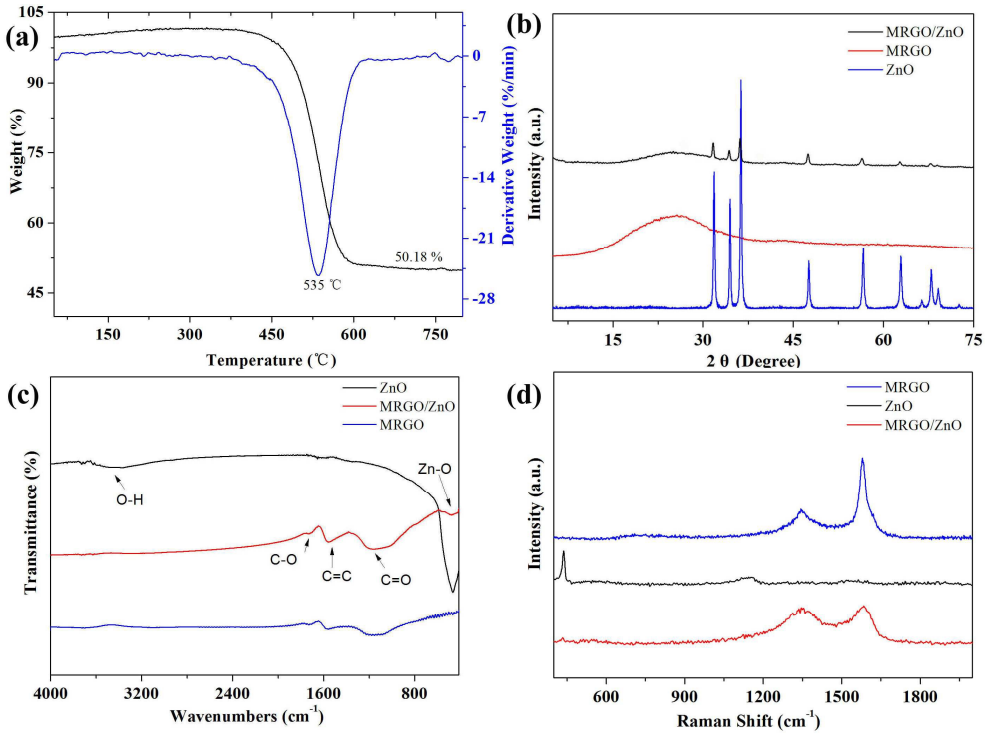

Fig. 3 (a) TG and DTG curves of MRGO/ZnO. XRD patterns (b), FTIR spectra (c), Raman spectra (d) of ZnO, MRGO and MRGO/ZnO

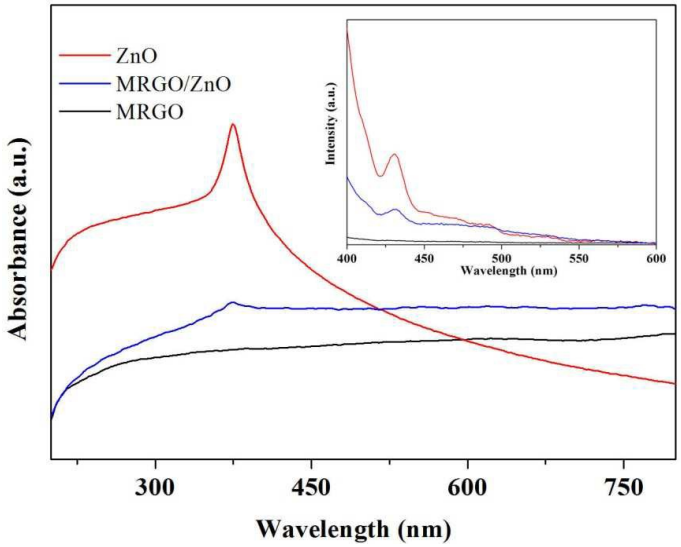

Fig. 4 UV-Vis absorption spectra of ZnO, MRGO and MRGO/ZnO. The inset shows the corresponding photoluminescence spectra.

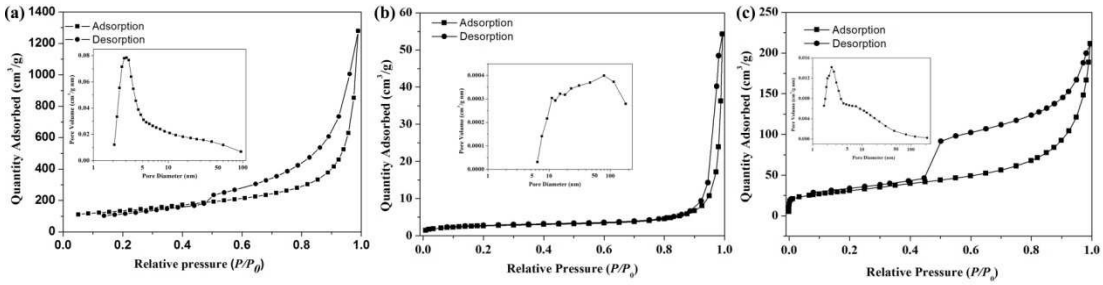

Fig. 5 Nitrogen adsorption isotherms of MRGO (a), ZnO(b) and MRGO/ZnO(c). The inset graphs are the pore size distribution.

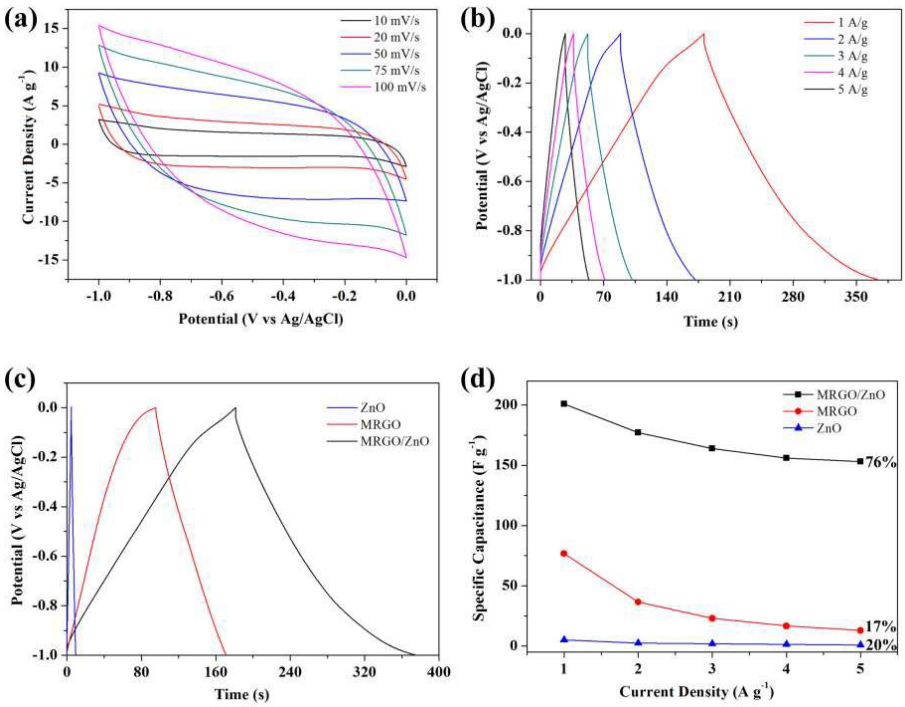

Fig. 6 (a) CV curves of MRGO/ZnO at different scan rates measured in a three-electrode system; (b) Galvanostatic charge–discharge curves of MRGO/ZnO electrode with different current densities; (c) Galvanostatic charge–discharge curves of different electrodes in 1 M Na_2SO_4 at a current density of 1 A g^{-1}; (d) Specific capacitance of ZnO, MRGO and MRGO/ZnO as a function of current density.

Table 1 Comparison of the specific capacitance of graphene-ZnO electrode with the reference

materials	synthetic method	specific capacitance	electrolyte	reference number
ZnO-graphene	Zn powder reduction	192 F g^{-1} (2 mV s^{-1})	KOH	50
graphene-ZnO film	ultrasonic spray pyrolysis	11.3 F g^{-1} (30 mV s^{-1})	1 M KCl	51
graphene-ZnO	ultrasonic spray pyrolysis	61.7 F g^{-1} (50 mV s^{-1})	1 M KCl	29
graphene/ZnO	microwave-assisted method	109 F g^{-1} (5 mV s^{-1})	1 M KCl	52
graphene /ZnO	thermal reduction	62.2 F g^{-1} (5mA cm^{-2})	1 M KOH	53
graphene-ZnO	hydrothermal reaction	156 F g^{-1} (5 mV s^{-1})	0.5 M Na_2SO_4	30
graphene-ZnO	microwave-assisted reduction	146 F g^{-1} (2mV s^{-1})	1 M KCl	54
graphene/ZnO	microwave irradiation	201 F g^{-1} (1 A g^{-1})	1 M Na_2SO_4	our work

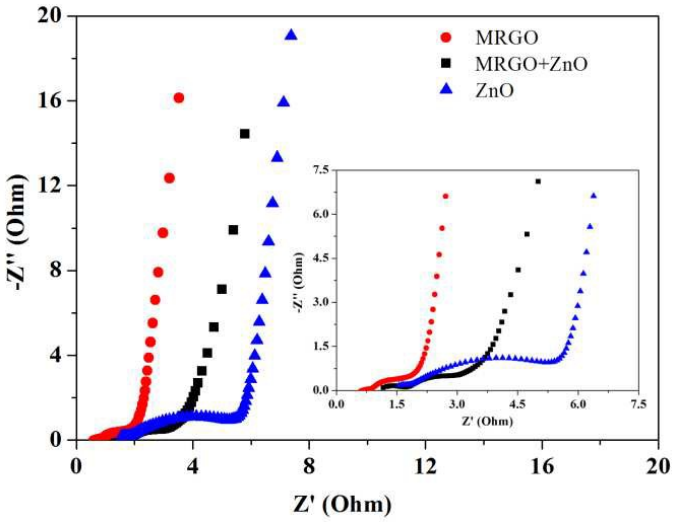

Fig. 7 Nyquist plots of MRGO, ZnO and MRGO/ZnO, inset is the expanded high-frequency region of the plots.

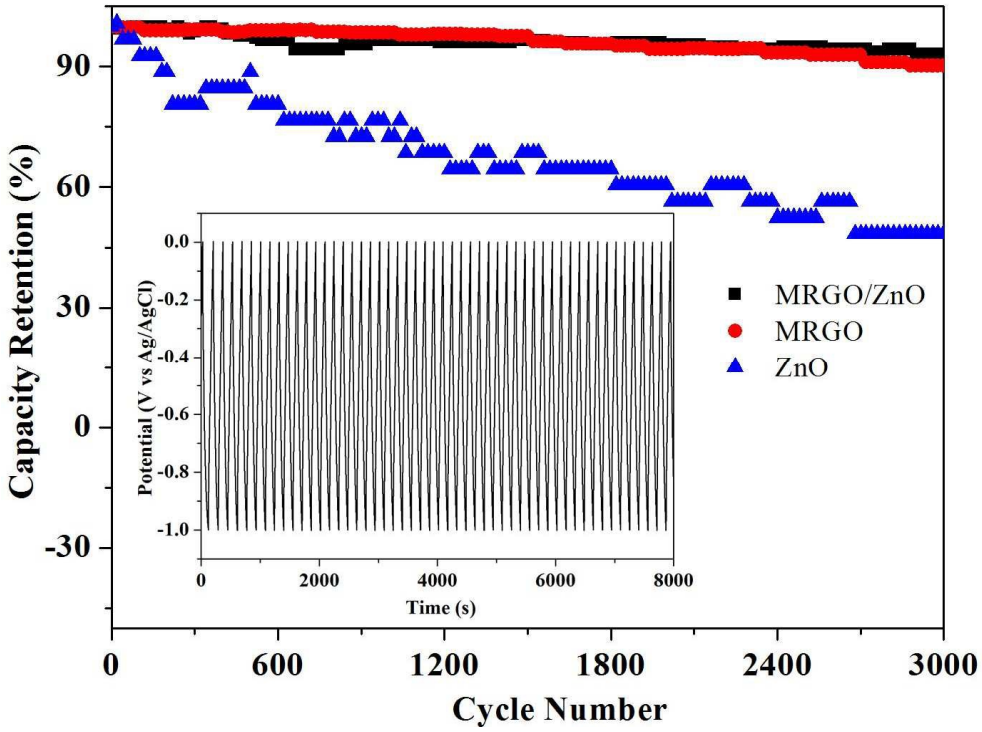

Fig. 8 Cyclic stability of MRGO, ZnO and MRGO/ZnO at a current density of 2 A g^{-1} for 3000 cycles.

Inset is the charge–discharge profile for the MRGO/ZnO electrode.

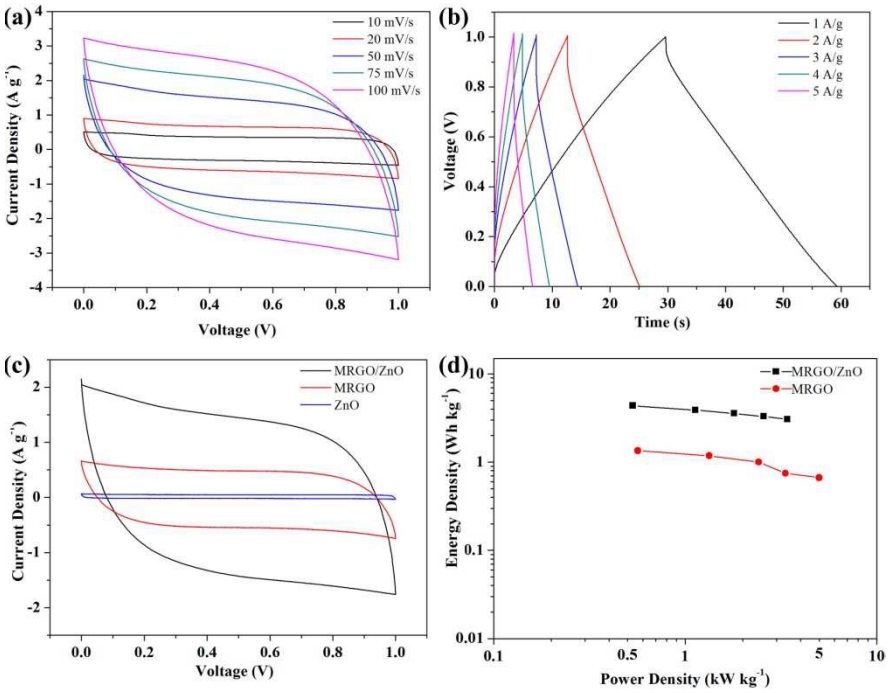

Fig. 9 (a) CV curves of MRGO/ZnO at different scan rates measured in a two-electrode system; (b) Galvanostatic charge–discharge curves of MRGO/ZnO electrode with different current densities; (c) CV curves of different electrodes at a scan rates of 50 mV s^{-1}; (d) Ragon plot of MRGO/ZnO and MRGO.